Journal of Nuclear Materials 539 (2020) 152320

Contents lists available at ScienceDirect

Journal of Nuclear Materials

journal homepage: www.elsevier.com/locate/jnucmat

Effects of Picture Frame Technique (PFT) on the corrosion behavior of 6061 aluminum alloy

Mariana X. Milagre [a, *], Uyime Donatus [b], Naga V. Mogili [c], Caruline S.C. Machado [a], Joao Victor S. Araujo [a], Rafael E. Klumpp [a], Stela M.C. Fernandes [a], José A.B. de Souza [a], Isolda Costa [a]

[a] *Instituto de Pesquisas Energéticas e Nucleares, IPEN/CNEN, Av. Prof. Lineu Prestes, 2242, São Paulo, Brazil*
[b] *Brunel Centre for Advanced Solidification Technology (BCAST), Brunel University, Uxbridge, Middlesex, UB8 3PH, UK*
[c] *Laboratório Nacional de Nanotecnologia, LNNano/CNPEN, Rua Giuseppe Máximo Scolfaro, 10.000, Polo II de Alta Tecnologia de Campinas, Brazil*

ARTICLE INFO

Article history:
Received 14 February 2020
Received in revised form
4 June 2020
Accepted 9 June 2020
Available online 22 June 2020

Keywords:
Aluminum alloys
Localized corrosion
Characterization

ABSTRACT

The 6061 Al–Mg–Si alloy is used in nuclear fuel plates of nuclear research reactors which are fed with fuel in plate shapes. The production of these plates is based on the picture frame technique (PFT). The picture frame technique (PFT) is a manufacturing process for the fabrication of nuclear fuel plates where the nuclear fuel is encapsulated by Al alloy plates and thermomechanically processed to generate a set with reduced thickness. The effects of PFT on the corrosion resistance of the 6061 aluminum alloy were evaluated in this study by immersion and electrochemical tests in 0.005 mol L^{-1} NaCl solution. The results showed that the PFT fabrication process increases the corrosion resistance of the 6061 alloy in relation to the conventional 6061-T6, due phase dissolution and lower content of β” phase. Also, corrosion propagation gradually changes, with an increasing number of processing steps, from intergranular to intragranular corrosion attack.

1. Introduction

The 6xx series aluminum alloys contain Si and Mg in their composition which favor magnesium silicide (Mg2Si) precipitation. Despite the low mechanical resistance of this series of alloy compared with the 2xx and 7xx series, this class of alloy presents good weldability, formability and corrosion resistance [1]. One of the alloys from the 6xx series, the 6061 alloy, finds large application in the fabrication of fuel plates for research nuclear reactors.

In the beginning of research nuclear reactors operation, pure aluminum was used in the fabrication of nuclear fuel plates. Studieds showed that even after being irradiated for more than 50 years at low temperature, the pure aluminum clad was found in good condition [2]. However, the 6061 Al–Si–Mg was introduced as nuclear clad application in the 50s [2] with the aim of to increase the corrosion resistance of the nuclear fuel plate at high temperature. Moreover, this alloy presents good radiation tolerance, even at low temperatures, and compatibility with the primary coolant used in nuclear reactors [3]. Other properties, such as low neutron absorption cross-section, good corrosion resistance and mechanical properties are cited as important for this type of application [4–6]. Usually, the 6061 aluminum alloy temper for the fabrication of nuclear fuel plates is either commercial extruded T6 temper or O temper. The 6061-T6 alloy presents good mechanical properties and corrosion resistance [1,7], which are important properties for application as structural nuclear case alloy, Fig. 1. The manufacturing process of 6061-T6 alloy comprises a step of solution heat treatment followed by an artificial aging step, where the alloy is heated at 175 °C for 10 h–20 h [8].

The precipitation sequence in the 6061 alloy was described by Edwards et al. [9]. Initially, from a supersaturated solid solution, clusters of Mg and Si precipitate individually. Subsequently, the Mg clusters dissolve and co-clusters of Mg and Si are formed. Guinier-Preston zones (GP zones) are thermodynamically more stable than the clusters, and, consequently, this transformation is easily promoted. These are the firsts steps in the precipitation sequence [10–14]. According to Andersen et al. [11,13,14], the β” (Mg5Si6) phase is the main phase responsible for the mechanical resistance of the 6061 alloy (peak-aged state). This phase has a needle-shaped

---

* Corresponding author.
E-mail address: marianamilagre@yahoo.com.br (M.X. Milagre).

https://doi.org/10.1016/j.jnucmat.2020.152320

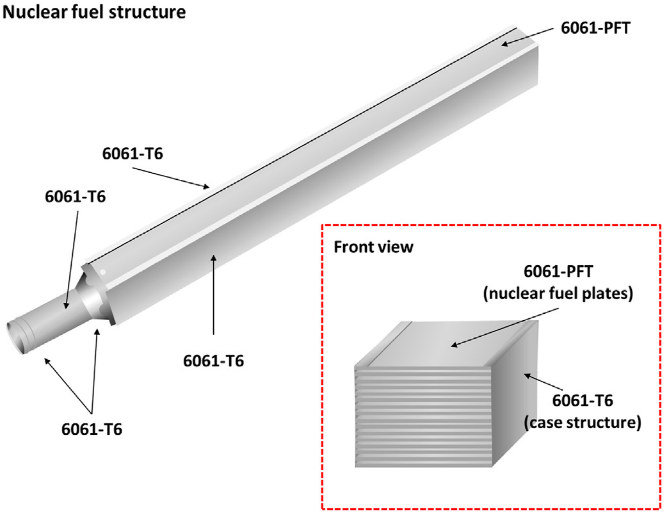

Fig. 1. Schematic diagram of the nuclear fuel plates case structure.

morphology and is aligned parallel to the (100)Al axis. β’ (Mg9Si5) phases is formed in the sequence (over-aged state) as rod-shaped phases [11,13,14]. Other phases such as Q’ ($Al_4Mg_8Si_7Cu_2$), can be also observed in this state [9–14]. Finally, in the equilibrium state, the β (Mg2Si) with plates or cubes of 10–20 μm morphology and face centered cubic (FCC) structure is observed [9,12].

The microstructure of Al alloys is influenced by the thermo-mechanical process to which they are subjected to Ref. [15–18]. The picture frame technique (PFT) is a manufacturing process for the fabrication of nuclear fuel plates. In this process, the nuclear fuel is encapsulated by 6061 plates to generate a set of 9 mm thick plates, which are further reduced to a thickness of 1.52 mm. Fig. 2 illustrates, in a schematic diagram, the fabrication stages of the nuclear plate fuels.

In the fabrication process of the nuclear fuel plates, specifically cladding and frame plates, the 6061 alloy is used in the O temper condition (1) due to its ductility. The plates are initially heated at 440 °C for 15 min for the thickness reduction of the as-received plates. The reduction in thickness occurs by 2–3 passes of hot rolling (2). In the sequence, their surfaces are treated according to a sequence of steps(3). The surface treatment steps include degreasing in acetone, pickling in NaOH (6–10 wt%) at 60 °C for 1 min, rinsing in flowing water for 1 min, immersion in HNO3 (30–50 vol%) for 1 min, rinsing in flowing water for 1 min, rinsing in deionized water, and drying under a hot airflow. Subsequently, the frame part is heated again (4) to allow the core fuel positioning by friction (5). Later, the cladding plates are positioned and fixed, and the edges are welded by TIG (tungsten inert gas) process in an argon controlled atmosphere (6). In the sequence, the nuclear fuel “sandwich” is heated to 440 °C for 60 min and, then, passes through the multi-pass hot rolling stage, whose parameters (temperature and number of passes) depend on the fuel composition, are carried out (7). For example, the production of the U3Si2–Al element requires between 7 and 9 hot rolling passes until an accumulated reduction in thickness of 81.9% is reached. In this case, the expected reduction in thickness for the first 2 passes is about 25% (per pass), whereas for the other passes a reduction of 15% is projected. Between the passes, the set is heated at 440 °C for 15 min. After hot rolling, the plates are heated to 440 °C for 60 min to check roll welding efficiency (8) and, then, the cold rolling stage is done (9). In the cold rolling stage, a reduction of 10% in thickness is required and, therefore, 1 to 2 passes are obligatory. At this stage, the accumulated reduction is about 83.5%. The core length of the fuel plate is then estimated to ensure that it has the minimum size required for application in nuclear reactors. Finally, the plates are flattened (10) for finishing, using a roll system in 1 pass and the edges are cut off to obtain the fuel plate with optimal dimensions. The plate surface is again treated according to stage (3). Finally, a nuclear fuel case composed of 18 nuclear fuel plates produced by the PFT process is set for operation in the reactor, as schematically shown in Fig. 1.

As described, the PFT process comprises cycles of heating and deformations which influence the alloy microstructure, promoting changes to the T6 and O temper conditions of the as-received alloy. Also, the corrosion behavior of the alloy is affected by the manufacturing process.

The effects of aging process on the corrosion behavior of the 6061 Al-alloy was reported by El-Menshawy et al. [19]. The authors evaluated the effects of heat treatment on the corrosion characteristics on the underaged, peak aged and overaged 6061 alloy using potentiodynamic polarization in neutral NaCl solution and immersion testing in acidified NaCl solution. The authors reported a significant dependence of corrosion morphology and electrochemical response on aging conditions. Moreover, since the corrosion mechanisms in the 6XXX Al-alloys involve trenching and de-alloying of micrometric and nano-sized particles, these particles are affected by mechanical and heating processes [20–24]. Micrometric particles are formed during casting, however, diffusion processes during aging have been related to compositional changes in the intermetallic particles and, thus, it must affect the alloy corrosion resistance [25]. Also, the morphology of nano-sized particles and their distribution are dependent on aging process.

The corrosion behavior of the 6061 alloy under PFT thermo-mechanical treatment conditions is of great importance for the definition of parameters to be used for fabrication of nuclear reactor components. Studies that investigate the effects of the PFT process on the corrosion behavior of the alloy are scarce, especially in solutions of low aggressiveness [26–28]. In this work, the effects of PFT on the corrosion behavior of the 6061 alloy was investigated in neutral 0.005 mol L-1 NaCl solution and correlated with the microstructural features of the plates in the O and T6 temper conditions of the as-received plates.

2. 2. Experimental

2.1. Materials

The composition of the 6061 alloy used in this study (Al 89.9 wt %, Cr 0.10 wt%, Cu 0.22%, Fe 0.20 wt%, Mg 0.90 wt%, Mn 0.05 wt%, Si 0.13 wt% and Zn 0.02 wt%) was evaluated, before and after the PFT process. Samples of the 6061 subjected to different stages of the nuclear fuel plate manufacturing process by picture frame technique (PFT) were used. Table 1 shows a summary of the thermo-mechanical history of each of the condition studied.

2.2. Microstructural characterization

The surfaces of the 6061 samples were prepared by mechanical grinding with SiC paper (#500, #800, #1200, #2500, #4000) with alcohol as a lubricant to minimize the effect of water on the corrosion process of Mg enriched particles. After grinding, the samples were polished with diamond suspensions of 3 μm and 1 μm. The microstructure of the plates was observed by optical microscopy after etching the sample in 10% NaOH solution at 60 °C for 30 s, followed by immersion in 30% HNO_3 and immersion in a 100 mL solution containing 4 g of $KMnO_4$ and 1 g of NaOH. Scanning electron microscopy (SEM) images were acquired using a Jeol JSM-6701F equipped with an energy dispersive X-ray detector (EDX).

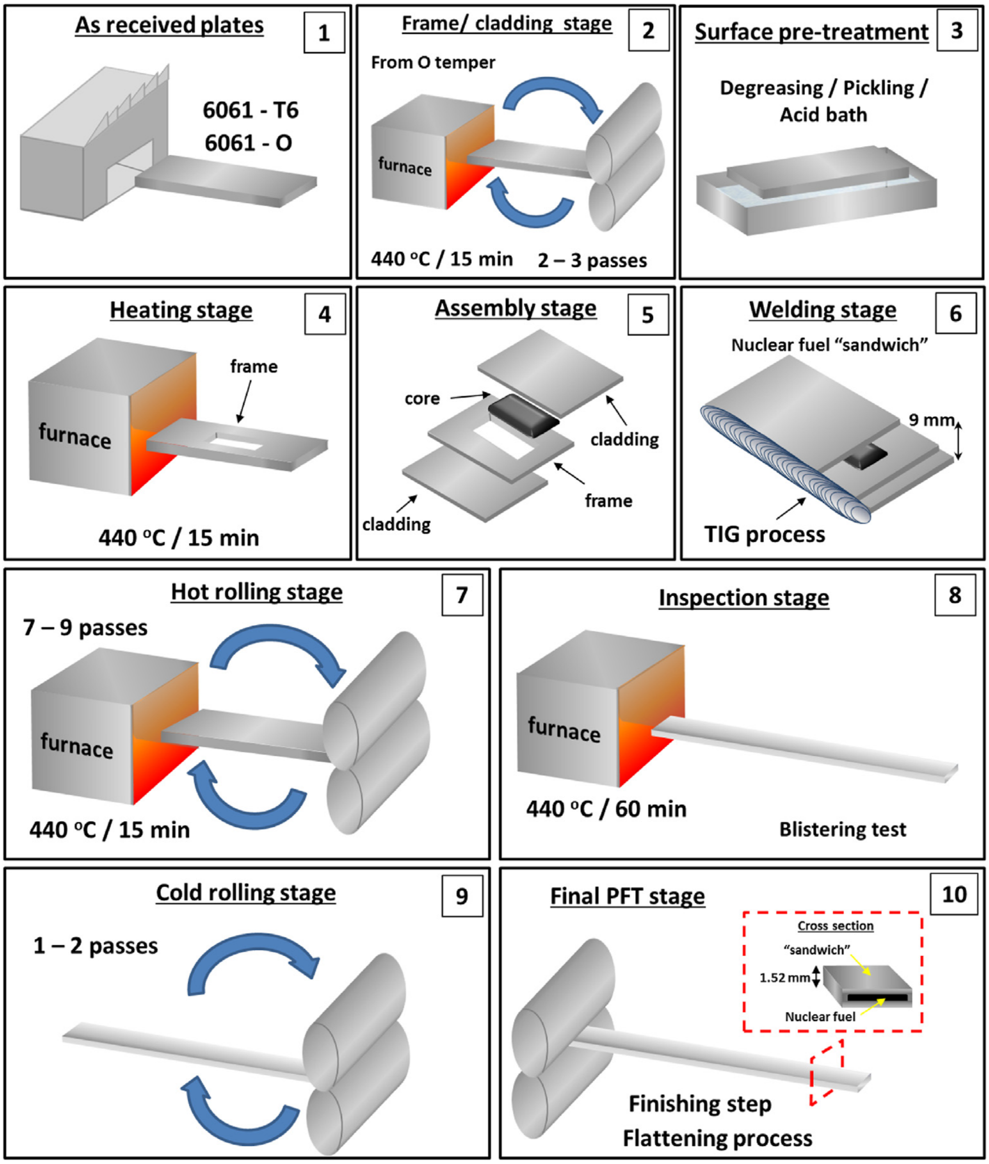

Fig. 2. Schematic diagram showing the stages for producing the nuclear fuel plates by the picture frame technique (PFT).

Table 1
Summary of the thermomechanical condition to which the 6061 alloy was exposed to at the different stages of the nuclear fuel plates manufacturing process by the picture frame technique (PFT).

	Description
T6	(1) Solution heat treatment followed by (2) artificial aging – commercial process.
O	(1) Annealing - commercial process.
Clad	(2) Thermal treatment (of O alloy) at 440 °C for 15 min followed by (3) Hot rolling (2–3 passes).
Inspection (Insp.)	(4) Heat treatment of the "fuel sandwich" (the clad) at 440 °C for 15 min followed by (5) hot rolling (7–9 passes) and (6) another thermal treatment at 440 °C for 60 min.
PFT	(7) Cold rolling (after "Inspection" stage) in 1 or 2 passes.

The electron microscope was operated using an incident beam of 15 kV. The particles fraction distribution was calculated using an image analyser software in an area of 227 μm × 184 μm. Transmission electron microscopy (TEM) analysis was carried out with samples mechanically polished and electropolished at 20 V in a solution of nitric acid (30 vol%) in methanol. TEM samples were prepared using TenuPol electropolishing equipment. Scanning transmission electron microscopy (HAADF-STEM) analysis was conducted using a Titan microscope equipped with EDX detectors.

2.3. *Differential Scanning Calorimetry (DSC)*

DSC data were obtained in nitrogen (99.999 wt%) atmosphere using an 822 Mettler Toledo equipment. Samples were ground with silicon carbide paper. The weights of the samples used in this test were in the range of 20 mg–30 mg. The heating rate used in the

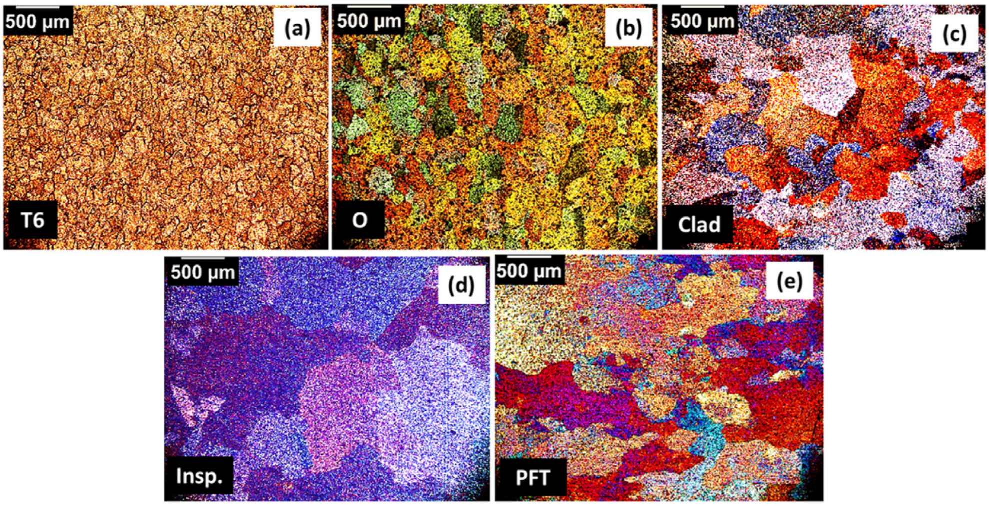

Fig. 3. Optical micrographs showing the grain morphology of the 6061 alloy. (a) T6 commercial temper; (b) O commercial temper; (c) Cladding (Clad) stage; (d) inspection (Insp); stage; (e) picture frame technique (PFT) final stage.

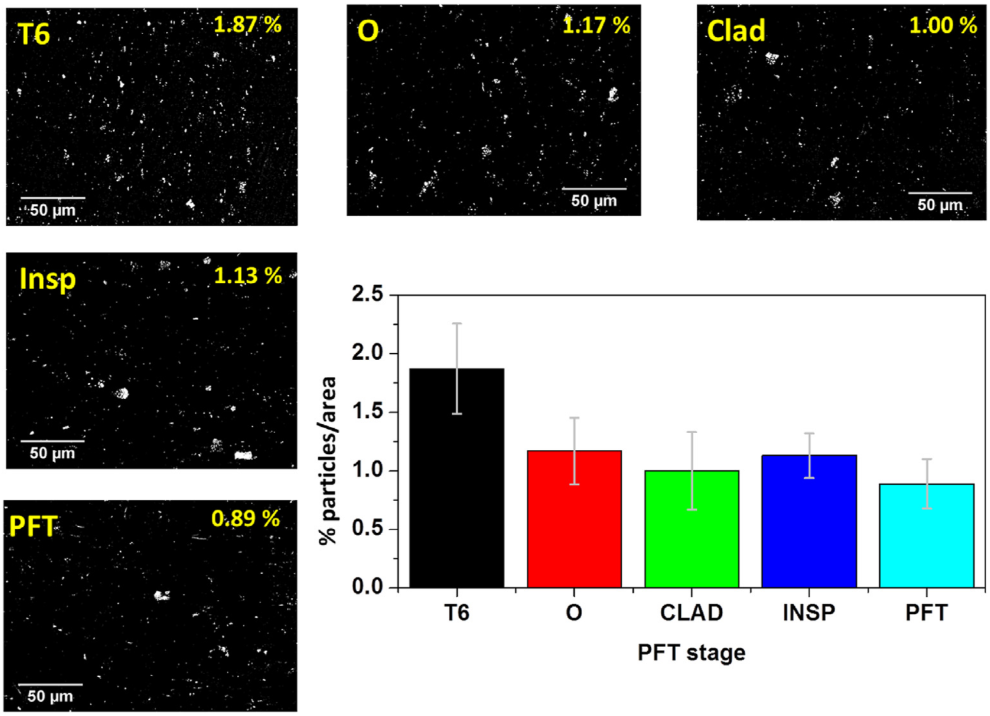

Fig. 4. Relationship between the PFT stages and the micromentric particles distribution.

DSC measurements was 10 °C/min and the scanning temperature range was from 25 °C to 550 °C.

2.4. Microhardness test

Microhardness measurements were recorded from the sample surface using a load of 200 gf for a dwell time of 10 s. A Buehler macrohardness machine was employed for this purpose. 30 random measurements were recorded at the surface of each sample, and their mean values were estimated.

2.5. Immersion test

The samples were also exposed to ASTM G110 intergranular corrosion test solution. For intergranular corrosion test, the surfaces of the samples were prepared according to the standard practice by (1) immersion for 1 min in the etching solution composed of 945 mL of deionized water, 50 mL of nitric acid (70%) and 5 mL of hydrofluoric acid; (2) rinsing in deionized water; (3) immersion for 1 min in concentrated nitric acid (70%); (4) rinsing in deionized water; and (5) drying under a hot air stream. After surface preparation, the specimens were immersed for 6 h in a solution comprised of 57 g NaCl and 10 mL H_2O_2 in 1 L deionized water

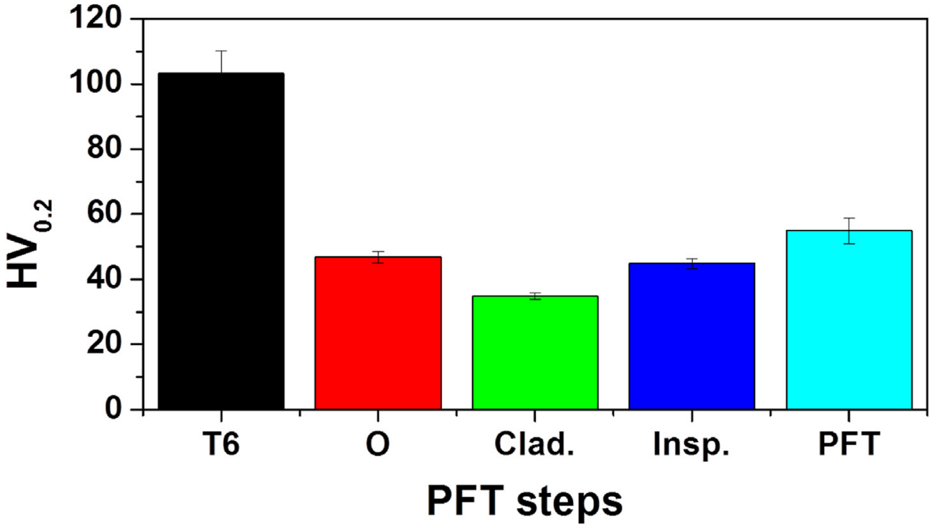

Fig. 5. Relationship between microhardness and the stages associated with the picture frame technique (PFT) for the 6061 alloy.

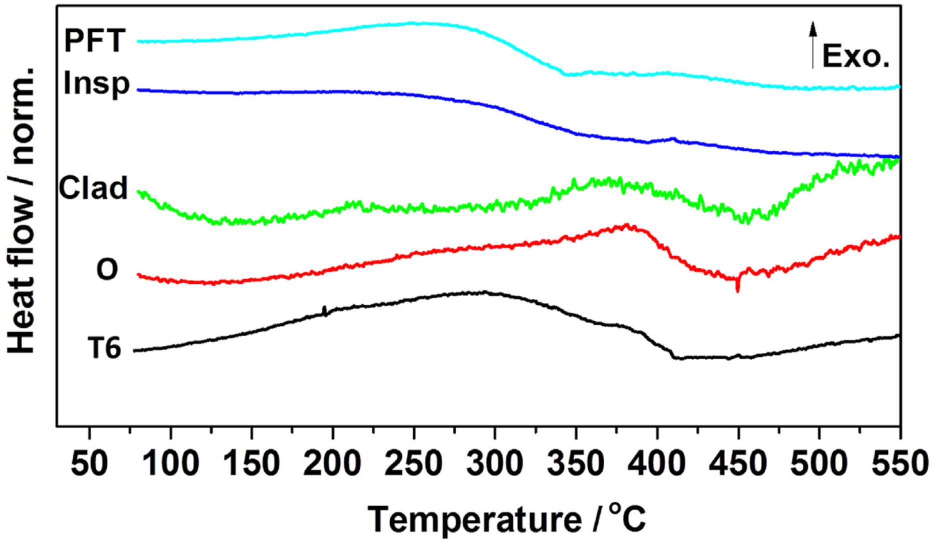

Fig. 6. DSC thermograms obtained at 10 °C/min from the 6061 alloy in different picture frame technique (PFT) stages. (a) T6 commercial temper; (b) O commercial temper; (c) cladding (Clad) stage; (d) inspection (Insp) stage; (e) picture frame technique (PFT) final stage.

at room temperature (22 ± 2 °C). The volume of the test solution to the area exposed to the test solution was 5 mL cm^{-2}. The exposed surfaces were observed by Scanning electro microscopy (SEM).

2.6. Electrochemical characterization

Potentiodynamic polarization and open circuit potential (OCP) measurements were obtained using an Autolab PGSTAT potentiostat controlled by NOVA 2.1 software. All measurements were performed at (22 ± 2) °C in naturally aerated 0.005 mol L^{-1} NaCl solution using a three-electrode set-up. An $Ag/AgCl_{KCl(sat)}$ electrode was used as the reference electrode, a platinum wire as counter electrode, and the Al alloy as the working electrode. The area of the working electrode exposed to the test solution was 0.09 cm^2. Polarization curves were obtained at a scan rate of 1 mV/s, from OCP to 1.3 V vs. Ag/AgClKCl(sat). Impedance electrochemical spectroscopy (EIS) measurements were obtained after 24 h of immersion in the test solution composed of at OCP with a signal amplitude of 20 mV. The frequency range scanned was from 10^4 Hz to 10^{-2} Hz.

3. Results and discussion

3.1. Microstructural characterization

Fig. 3 shows the changes in the microstructural features of the 6061 Al–Mg–Si alloy with the thermomechanical process. In the T6 temper, Fig. 3(a), the grains are smaller compared to the other tested conditions. The O temper corresponds to the industrial temper related to the lowest strength. In this temper, the alloy is annealed to increase ductility that is suitable for severe forming applications. As observed in Fig. 3(b), the grain shape is larger than in the T6 condition due to heating. The PFT stages modify the grain morphology of the 6061 alloy. In the Clad sample, Fig. 3(c), the grains are larger than for the T6 and O samples. As previously reported, to obtain the cladding of the nuclear fuel sandwich, the alloy in the O or T6 condition is heated at 440 °C for 15 min and hot

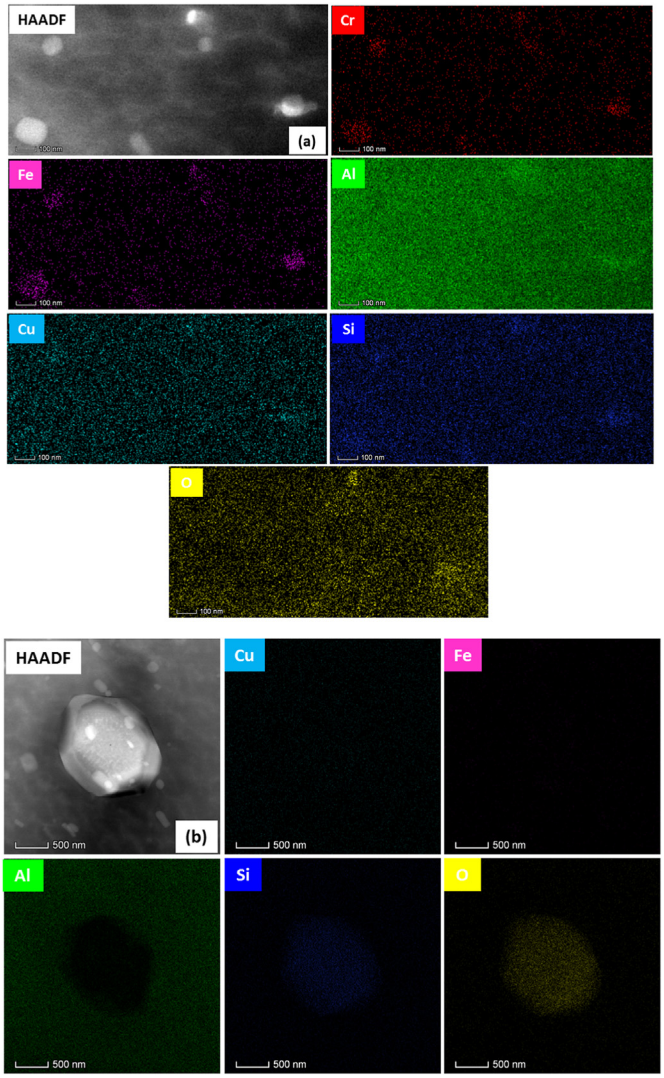

Fig. 7. HAADF-STEM images and EDS analyses of the nano-sized particles present in 6061 alloy. (a) Fe–Si–Cr–Cu enriched particles; (b) Si enriched particles.

rolled in 2 or 3 passes. The Inspection sample, Fig. 3(d), showed the largest grains. It is important to highlight the thermomechanical process that this kind of sample was exposed to. The sandwich was heated at 440 °C for 15 min, hot rolled in 7 or 9 passes and again heated at 440 °C for 60 min which resulted in grain growth. Finally, the PFT sample, Fig. 3(e), which represents the final thermomechanical condition of the nuclear fuel plate, presents smaller grains than the inspection sample, due to 1 or 2 cold rolling passes after the inspection stage.

The effects of the fabrication process on the distribution of the micrometric particles were also evaluated, Fig. 4. From the observation of surfaces of the samples, Fig. 4(a-e), the extruded alloy, T6 temper, showed the highest amounts of micrometric phases per area among the conditions tested. Moreover, for all the conditions, the particles are evenly distributed over the surface. In addition, the PFT process did not change the distribution of the particles in relation to the as-received condition (O temper) as seen in Fig. 4(f). The error bars corresponding to the O and PFT samples are overlapped.

In terms of mechanical properties, the PFT stages reduced the hardness of the 6061 alloy in relation to the T6 temper, Fig. 5. However, in relation to the O temper, the PFT process increased the alloy hardness and, therefore, the strength of the alloy in the last stage of the process (PFT sample), due to cold rolling. In the Clad condition, the plate presented the lowest hardness. The phase responsible for the optimal strength of the Al–Mg–Si alloys is the β” phase [11,29]. This phase presents a needle-like morphology coherent along its length with the matrix, which is aligned parallel to $<100>_{Al}$ and it usually precipitates at temperatures in the range of 125 °C–200 °C [9,11,30–37]. Since dislocations are preferential sites for phase precipitation, there is a deformation field associated with the formation of GP zones, which is progressively relieved as the zones are transformed into semi-coherent β′ or incoherent β precipitates, and, consequently, the strength is reduced [32,35]. The meta stable Q’ phase, which has a composition close to $Al_4Mg_{8-}Si_7Cu_{2,}$ is reported to increase the hardness of the 6061 alloy [19,38]. This phase is found in Cu containing 6XXX series alloy. It has a lath-shaped hexagonal structure aligned parallel to the $<100>_{Al}$ and is a precursor of the Q ($Al_4Mg_8Si_7Cu_2$) phase [11,38].

In order to correlate microhardness with phase dissolution/precipitation, DSC curves were obtained, Fig. 6. The typical T6 temper involves solution heat treatment, quenching and aging at temperatures within 175 °C–180 °C for 10–20 h [11]. The DSC thermograms for the T6 condition showed a dissolution peak between 300 °C and 350 °C. The exothermic peaks in the DSC thermograms are related to the elements in solid solution which, during heating, might form precipitates according to the alloy precipitation sequence. The precipitation sequence proposed for the Al–Mg–Si–Cu alloys [39] is shown in equation (1) below.

$$SSS \rightarrow clusters \rightarrow \ GP\ zones \rightarrow \ \beta^{''} + Q^{'} \rightarrow \ \beta + Q \qquad (1)$$

According to the literature [11,37], for Al–Mg–Si alloys, a peak between 60 °C and 80 °C is associated with clusters of Si and Mg that correspond to aggregates of disordered solute atoms. According to Buha et al. [11], these clusters have higher contents of Mg in relation to Si. Nonetheless, these precipitates are unstable and dissolve when the alloy is exposed to heating between 190 °C and 235 °C [11]. The absence of this peak for the T6 temper, shows that the formation of clusters had finished and the slight decrease in the base line is probably due to dissolution of small clusters without enough energy to nucleate as GP zones. At the range of 150 °C and 250 °C, the GP zones are formed [11,36]. This phase differs from the clusters of Si and Mg in terms of number of solute atoms and size, with less Mg in their aggregates compared to the clusters [11]. The absence of this peak confirms the GP zones as precursors for the β” phase (and its completely phase precipitation) [11,36]. The T6 temper is a peak aging condition and, according to the literature [38], the precipitation of β” is completed in Cu-containing aluminum alloys in this condition, though incomplete for Q′ phase. Thus, the broadened peak observed in the range of 250 °C and 350 °C is related to the Q′ phase [38]. Between 350 °C and 450 °C, β′ precipitates are formed [32,36], although the Q phase formation is also reported for Cu containing alloys [38]. Since β” is favored in T6 temper, and this phase is a precursor to β′, the heating input favors coarsening of β” which makes it to partially lose its coherence with the matrix leading to β′ formation. This phase is formed at temperatures in the range of 260 °C and 320 °C [32,36]. Finally, starting from 450 °C, a slight peak associated with the equilibrium phase β (Mg_2Si) is observed [32,36,38]. The O temper sample showed a different thermogram, which indicates a change in reaction kinetics. In the annealed condition, the 6061 alloy is ductile, Fig. 5, due the recristalization process, once high temperatures are used in this process, below the eutectic line [39]. Therefore, the strengthening phases (β” and Q′) are dissolved and hardness is reduced. The slight peak around 200 °C and 300 °C indicates the presence of the hardening phases. Moreover, the

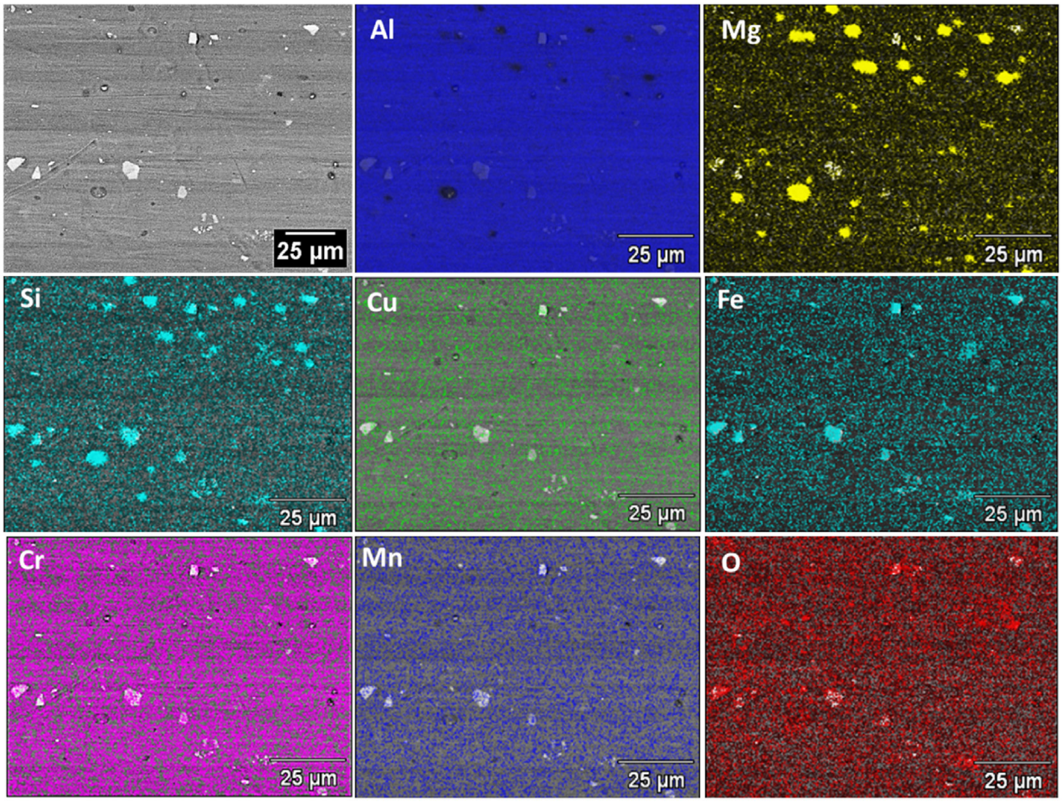

Fig. 8. (a) EDS maps of the 6061 alloy showing the chemical composition of the micrometric particles.

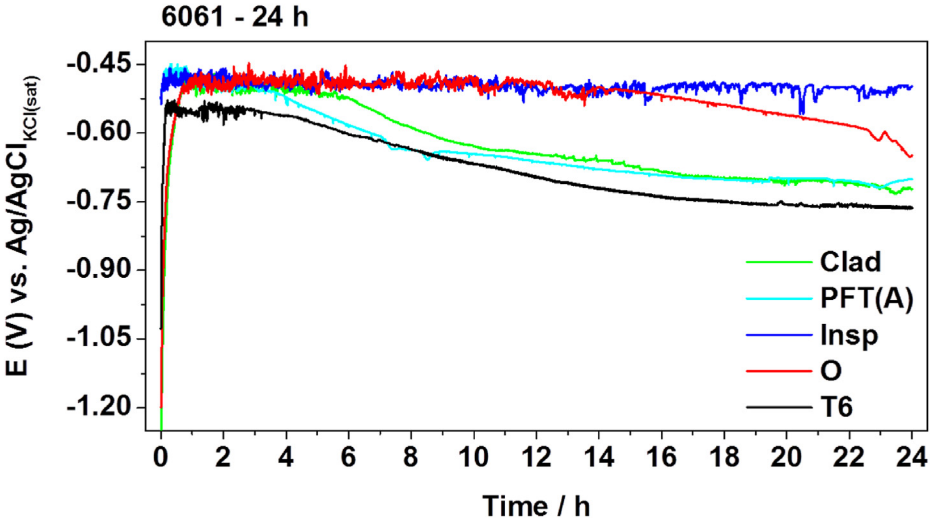

Fig. 9. Potential *vs.* time curves for the 6061 alloy in different stages of the picture frame technique during 24 h of immersion in 0.005 mol L^{-1} NaCl solution.

higher peak starting at 350 °C and 450 °C related to T6 temper is probably due to precipitation of Q and β'/B phases and non-dissolved precipitates coarsened during this treatment. The non-dissolved stable phase β, also coarsened, is responsible for the highest peak at 450 °C–550 °C.

The PFT process also promotes changes in precipitation reaction kinetics. The Clad corresponds to the stage in which the samples are heated to 440 °C for 15 min followed by 2 or 3 passes of hot rolling. This condition presented an exothermic peak around 200 °C–250 °C indicating that β'' and Q' phases precipitation are not favored in this stage of fuel production. Thus, more elements are in solid solution for this condition. Moreover, the lowest hardness values support these results indicating the dissolution of strengthening phases during this stage. The increment of the peak related to Q, β′ and β also indicate coarsening of non-dissolved precipitates. This result is supported by the reduction in microhardness and decreased mechanical resistance [9,33,40]. When these phases are present in the structure, heating after homogenization promotes either their coarsening or transformation (such as from β′ to β) [33]. The maximum hardness is reached when the

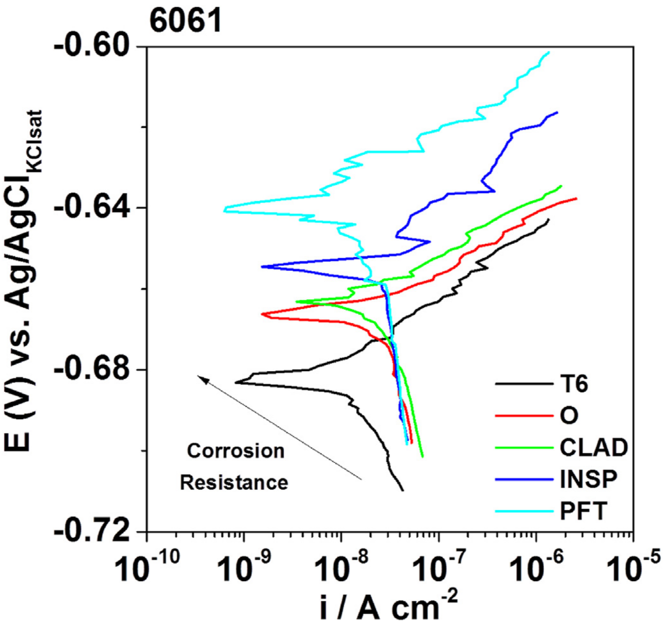

Fig. 10. (a) Anodic polarization curves of the 6061 Al–Mg–Si alloy in different picture frame technique (PFT) stages obtained after 30 min of immersion in 0.005 mol L^{-1} of NaCl solution.

alloy is homogenized before aging, T6 condition. Thus, the lower hardness related to the conditions of the PFT stages must be due to the presence of Q, β' or stable β phases [33].

For the inspection condition, the peak related to β" and Q′ phases and the higher microhardness than the Clad condition indicate that precipitation of these phases is favored during this stage. Microhardness of the inspection sample was higher than that of the Clad condition, even after heating at 440 °C for 60 min and showing the largest grain size, Fig. 3(d). The hardening during hot rolling, by the increases dislocations density, seemingly favored the precipitation of hardening phases [35,37,41,42]. The absence of peaks related to Q, β' and β phases explains the increased hardness in relation to the Clad sample. Lastly, in the final PFT stage, a large amount of elements seemingly is still in solid solution. Hardness of the final PFT sample increased in relation to the samples of other PFT stages, and this is related to the cold rolling process that favors increase in dislocation density and precipitation of the hardening phases, as presented in Fig. 4.

TEM analysis, Fig. 7, show typical nano-sized particles in the 6061 alloy. The particles were enriched in Cr, Fe, Cu and Si. The presence of Cr, Fe and Si in the constituent particles is due to their low solubility and low diffusion rate in Al matrix. Cr is known as a grain refiner and it is also added to improve the corrosion resistance of Al alloys [43,44]. Fe is known as an impurity element [39,45–48]. The addition of Cu can also improve the mechanical properties of the alloy by precipitation of strengthening phases, but it usually reduces the corrosion resistance of 6XXX Al-alloys [39,49]. Si is added to Al–Mg–Si alloys to increase their mechanical strength. Depending on the heat treatment used, different amounts and sizes of Mg–Si particles will be present in Si-containing Al-alloys. Particles with micrometric sizes are also present in 6061 alloy. Fig. 8 shows EDX maps indicating the chemical composition of micrometric particles present in the alloy.

The 6061 micrometric particles are, usually, Fe–Si or Mg–Si enriched. These particles are also known as intermetallics (primary impurities) in the microstructure of the Al–Si–Mg matrix. They are formed in the interdendritic regions during solidification or in the solid state during solution treatment, homogenization, or recrystallization. Despite the fact that these impurities have been reported as deleterious for mechanical properties (as sites for crack initiation and decohesion failure), depending on their chemical composition, they can show resistance to corrosion and oxidation due to their adherent surface oxides [40,50].

3.2. Corrosion characterization

Open circuit potential (OCP) measurements were recorded for all the conditions tested as a function of time of immersion in 0.005 mol L^{-1} NaCl solution for 24 h, and the results are presented in Fig. 9. Similar shapes were obtained for all conditions. Initially, a sharp increase in OCP was observed. This initial sharp increase in potential has been related to the oxide film growth naturally formed over the aluminum surface in contact with the electrolyte [51–53]. Once pitting potential is reached, oxide film breakdown occurs. Secondly, OCP oscillations at potentials above −0.57 V are observed indicating localized attack (pitting). The events leading to potential transients during free corrosion of Al alloys were discussed by Isaac et al. [53]. According to authors, the noise produced during Al alloys exposure to chloride solutions arises due to active sites where pit growth processes are occurring. Moreover, pits tunneling can be changed by many circumstances which explain the differences seen in the curves oscillations for each sample condition. Finally, OCP values decreased with time, which is related to constant surface activation.

The differences in OCP values for the various conditions tested after 24 h of exposure to the electrolyte indicate that the thermomechanical treatments involved in the fabrication of nuclear plates by PFT affect the electrochemical behavior of the exposed surfaces. This is also evident from the differences in the microstructures according to the thermomechanical treatments. Eckermann et al. [20] found nobler and more stable OCP values associated with naturally aged alloy (with a small number of MgSi precipitates) in relation to heat-treated one. The nobler OCP values associated with the PFT stage and O temper samples compared to the T6 one may be attributed to phase dissolution and lower content of precipitates related to those conditions [19,54]. The literature also reports potential ennoblement due to precipitate coarsening [54].

Fig. 10 shows the anodic polarization curves for the various 6061 samples after 30 min of immersion in 0.005 mol L^{-1} NaCl solution. In general, the PFT process increased the corrosion resistance of the 6061 alloy in relation to the as-received, T6 and O conditions. The corrosion pathways in the different 6061 samples after anodic polarization are shown in Fig. 11. The 6061-T6 alloy, Fig. 11(a), showed susceptibility to intergranular corrosion. For the other conditions, pitting and filiform-like corrosion were the main types of attack, Fig. 11(b–e). Corrosion propagation seems to change from intergranular corrosion mechanism to an intragranular corrosion type. In general, the corrosion mechanism in 6XXX alloys is associated with (1) Fe-enriched particles which are cathodic to the matrix and the (2) Mg–Si particles which have an ambiguous behavior [20,22,23].

Fig. 12(a) shows the surface of the 6061-T6 alloy after anodic polarization. Corrosion occurs at areas surrounding Fe-enriched micrometric particle, Fig. 12(b), which is cathodic to the matrix. Microgalvanic cells are established between this kind of particle and the surrounding matrix, during the OCP measurement period, leading to localized attack, known as trenching. Mg–Si particles being anodic to the matrix, are totally and/or partially consumed. The selective dissolution of Mg, a highly active element, leads to a remaining Si-enriched particle at the exposed surface and, consequently, polarity reversal, with the matrix becoming anodic to the Si-enriched particle resulting in cavities at the surface, that is, to

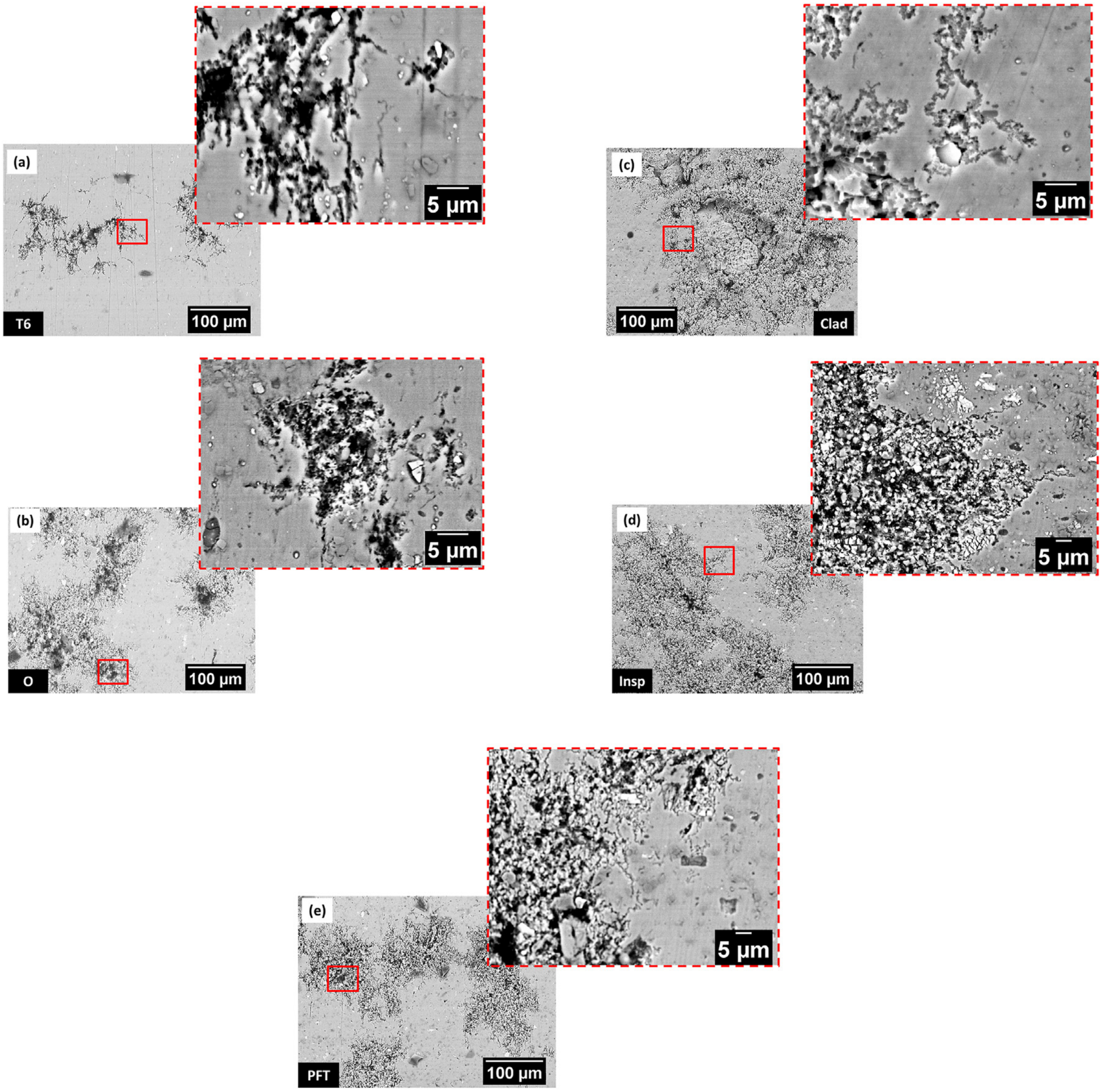

Fig. 11. SEM images of the anodic sites after 30 min of exposure to 0.6 mol L^{-1} NaCl solution at OCP followed by anodic polarization; (a) T6 temper; (b) O temper; (c) cladding (Clad) stage; (d) inspection (Insp.) stage, and (e) picture frame technique (PFT) final stage.

trenching.

According to Guillaumin et al. [23], intergranular attack in 6XXX alloys starts at the pit walls and corrosion spreads from the pit through grain boundary pathways. According to these authors, pits nucleated on and/or around Mg—Si particles. Also, they proposed that intergranular corrosion occurred due to preferential dissolution of precipitate free zones (PFZ) along grain boundaries, since for the 6056 alloy studied in their work, the particles at grain boundaries are Si—Cu enriched (being a high Cu-content alloy), whereas the regions surrounding these precipitates are depleted in these elements. In this study, the grain boundary particles comprised MgSi particles, that are anodic to the matrix of the 6061-T6 alloy. Mg—Si particles are predominant in the alloy of this study because 6061 is a lean alloy with lower Cu-content compared with the 6056 alloy. Therefore, the particles at the grain boundaries will dissolve preferentially, resulting in intergranular corrosion. This attack is favored when cathodic Fe-enriched particles are close to the grain boundary particles, as shown in Fig. 12. Herwever, due to the PFT process, precipitation of the anodic phases is favored inside the grains.

The corrosion mechanism of the 6061 alloy was also evaluated by electrochemical impedance spectroscopy (EIS) after 24 h of immersion in 0.005 mol L^{-1}, Fig. 13. All the curves presented similar shapes suggesting similar mechanisms for all the samples with differences only in the magnitudes of impedance. The results indicated two time constants. In the Nyquist diagrams, all the samples presented a flattened capacitive arc at high to medium frequencies which were related to the interaction between the thin oxide film at the surface and charge transfer processes coupled to charging of the double layer. At low frequencies, the EIS results suggest the presence of diffusion controlled corrosion processes. Despite the contribution of these processes at low frequencies, there is also contribution of other factors, since the slope of |Z| vs. frequency plot related to diffusion controlled processes is around 0.5 and the phase angle value is about 45° [55]. For the 6061 samples tested, the slope of |Z| vs. frequency plot is in the range between 0 and 0.5. The EIS results also showed impedances in the same range, tenths of kΩ.cm^2, for all tested conditions. Consequently, significant differences between the varios conditions tested were not clearly identified by EIS tests.

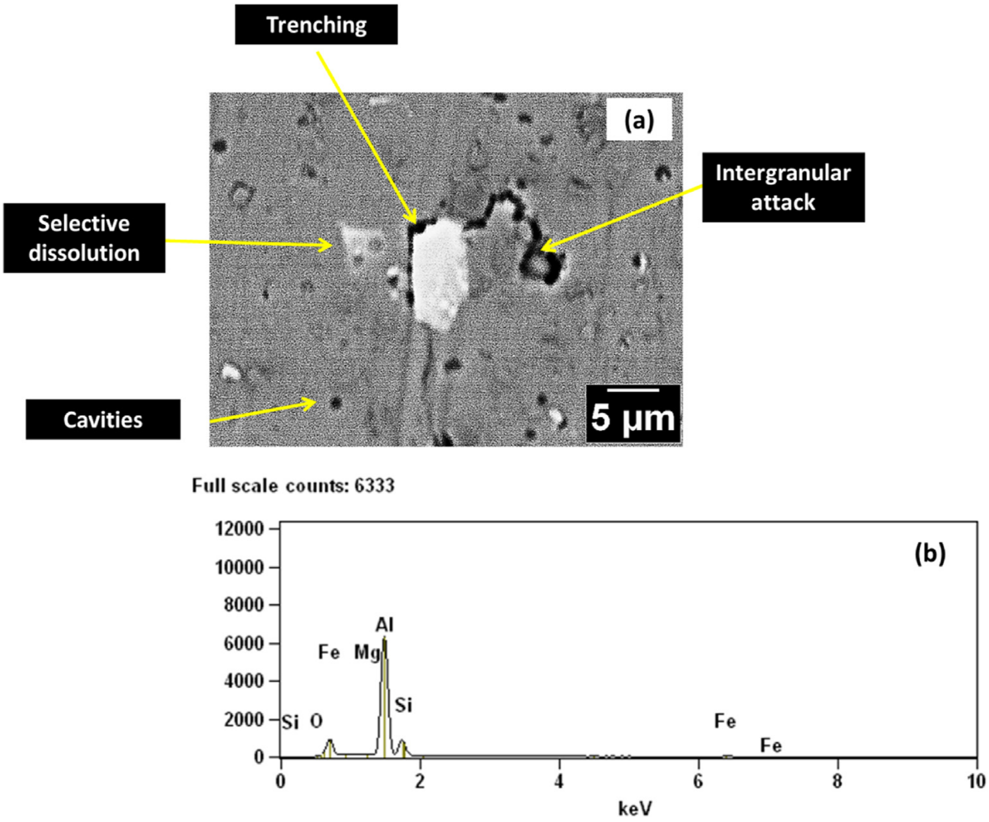

Fig. 12. (a) SEM image of the exposed surface of 6061-T6 after polarization showing the corrosion features associated with the micrometric particles; (b) EDX analysis of the Fe—Si enriched micrometric particle.

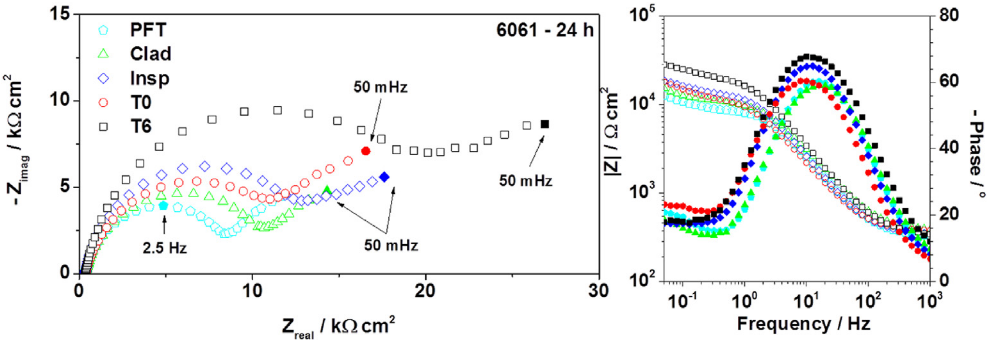

Fig. 13. EIS diagrams obtained for 6061 alloy in different picture frame technique (PFT) stages immersed in 0.005 mol L^{-1} NaCl solution for 24 h.

In order to confirm the differences in the intergranular corrosion susceptibility of the 6061 alloy for the different stages of the PFT process, the samples were exposed to the ASTM G110 standard practice solution for 6 h. Surface features of the tested samples after immersion are shown in Fig. 14. The results are in accordance with Fig. 11. The T6 temper exhibited the highest susceptibility to intergranular corrosion among the tested ones, Fig. 14(a). Intragranular attack was observed for the other conditions due to precipitation of anodic phases inside the grains, Fig. 14(b—e). Despite the intergranular corrosion observed for the O temper (Fig. 11(b)), and Clad stage (Fig. 11(c)), intragranular attack was the main mechanism of corrosion propagation in the PFT conditions. Cross-section images also confirmed the transition from intergranular to intragranular attack for the PFT 6061 samples, Fig. 15. The features observed after intergranular corrosion test provided useful information on the type of corrosion mechanism related to the microstructure resulting from the different types of thermo-mechanical treatments to which the various types of samples were exposed.

4. Conclusions

In summary, according to open circuit potential (OCP) measurements and polarization curves the thermomechanical processes involved in the picture frame technique (PFT) results in increased corrosion resistance of the 6061 alloy in relation to as-received T6 temper condition. Electrochemical impedance spectroscopy (EIS) results suggested similar electrochemical mechanisms of corrosion for all tested conditions. Corrosion propagation in the 6061-T6 alloy was mainly through grain boundaries

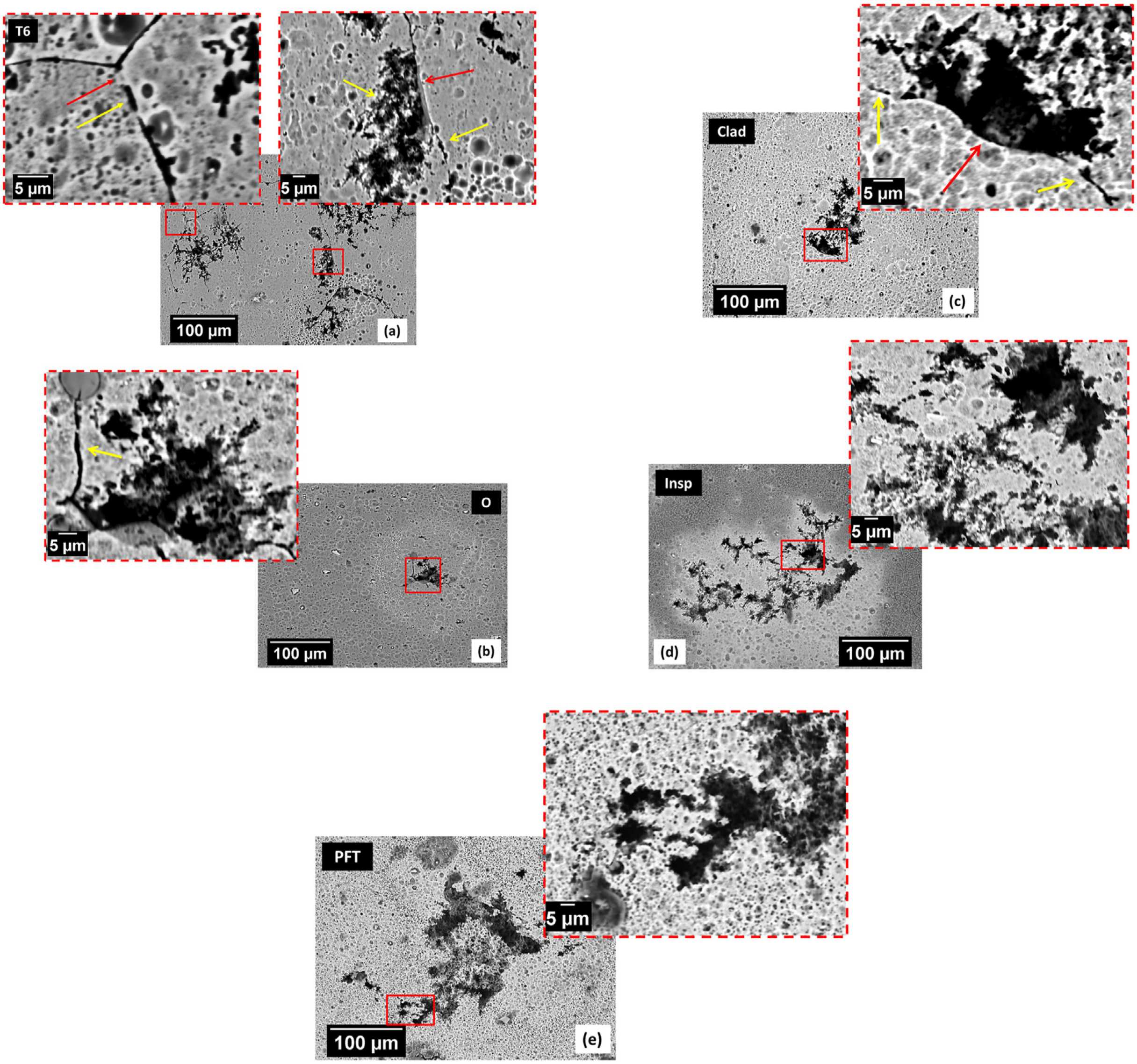

Fig. 14. SEM images of 6061 in different picture frame techniques (PFT) stages exposed to a solution composed of 57 g of NaCl and 10 mL of H_2O_2 in deionized H_2O to complete 1 L (ASTM G110) for 6 h. (a) T6 commercial temper; (b) O commercial temper; (c) cladding (Clad) stage; (d) inspection (Insp) stage; (e) picture frame technique (PFT) final stage.

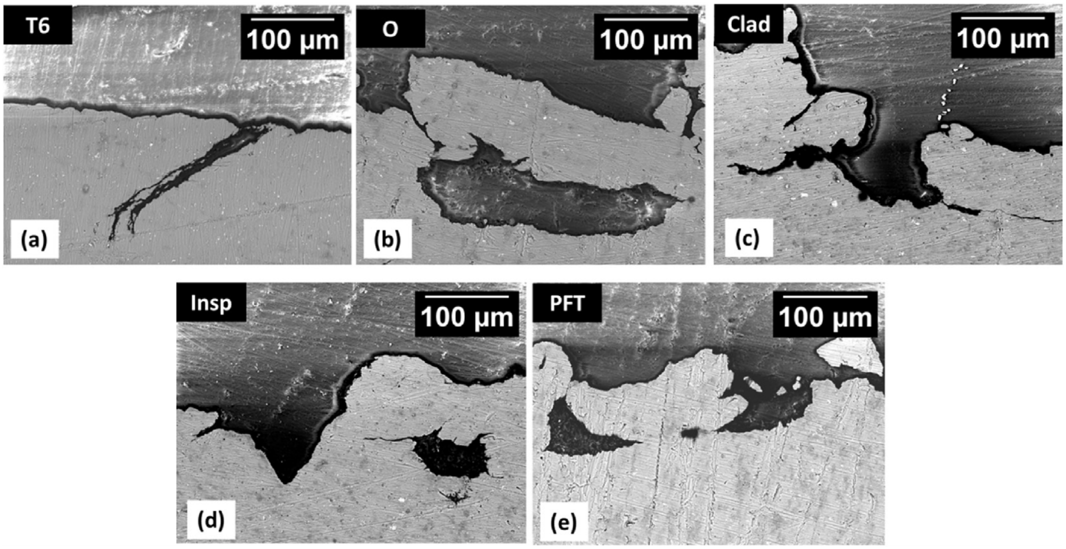

Fig. 15. Cross section SEM images of 6061 in different picture frame techniques (PFT) stages exposed to a solution composed of 57 g of NaCl and 10 mL of H_2O_2 in deionized H_2O to complete 1 L (ASTM G110) for 6 h. (a) T6 commercial temper; (b) O commercial temper; (c) cladding (Clad) stage; (d) inspection (Insp) stage; (e) picture frame technique (PFT) final stage.

(intergranular). The corroded surfaces and cross-section observations after exposure to test solutions showed that the mechanism of corrosion propagation varied from intergranular, in the case of T6 temper, to intragranular type, for the samples corresponding to PFT stages.

Data availability

The raw/processed data required to reproduce these findings cannot be shared at this time as the data also forms part of an ongoing study.

Acknowledgements

The authors acknowledge the National Comission for Nuclear Energy (CNEN) in Brazil for financial support to this work and for the grant of Mariana X. Milagre (SEI 01342.002357/2019–32). Acknowledgements are due to Dr. Duclerc Fernandes Parra and Dr. Margarida Mizue Hamada, from Nuclear and Energy Research Institute (IPEN/CNEN-SP) for technical support with DSC analysis and to LNANO/CNPEM, Brazil, for technical support with TEM analysis.

Appendix A. Supplementary data

Supplementary data to this article can be found online at https://doi.org/10.1016/j.jnucmat.2020.152320.

References

[1] ASM Handbook Properties and Selection: Nonferrous Alloys and Special-Purpose Materials, ASM International, 2001. http://books.google.com.hk/books?id=eC-Zt1J4oCgC.

[2] D. Féron, Overview of nuclear materials and nuclear corrosion science and engineering, Nucl. Corros. Sci. Eng. (2012) 31–56, https://doi.org/10.1533/9780857095343.1.31.

[3] R.H. Howard, R.C. Gallagher, K.G. Field, Mechanical performance of neutron-irradiated dissimilar transition joints of aluminum alloy 6061-T6 and 304L stainless steel, J. Nucl. Mater. 508 (2018) 348–353, https://doi.org/10.1016/j.jnucmat.2018.05.070.

[4] S.M.D.C. Fernandes, O.V. Correa, J.A.B. De Souza, R.A. Antunes, N.B. De Lima, L.D.V. Ramanathan, Effect of processing on microstructure and corrosion mitigating properties of hydrotalcite coatings on aa 6061 alloy, Mater. Res. 18 (2015) 1203–1208, https://doi.org/10.1590/1516-1439.015715.

[5] A.F. Forte Giacobone, S.A. Rodriguez, A.L. Burkart, R.A. Pizarro, Microbiological induced corrosion of AA 6061 nuclear alloy in highly diluted media by Bacillus cereus RE 10, Int. Biodeterior. Biodegrad. 65 (2011) 1161–1168, https://doi.org/10.1016/j.ibiod.2011.08.012.

[6] I.M. Elseaidy, M.M. Ibrahim, M.M. Ghoneim, M.E.A. El-Azim, Aluminum alloys strengthening by accumulative roll- bonding (arb) process, in: Trans SMiRT (Ed.) 19, 2007, pp. 1–10. Toronto.

[7] C. Vargel, M. Jacques, D. Schmidt, The most common wrought aluminium alloys, Corros. Alum. (2004) 61–69.

[8] S. Pogatscher, H. Antrekowitsch, H. Leitner, T. Ebner, P.J. Uggowitzer, Mechanisms controlling the artificial aging of Al-Mg-Si Alloys, Acta Mater. 59 (2011) 3352–3363, https://doi.org/10.1016/j.actamat.2011.02.010.

[9] G.A. Edwards, K. Stiller, G.L. Dunlop, M.J. Couper, The precipitation sequence in Al-Mg-Si alloys, Acta Mater. 46 (1998) 3893–3904, https://doi.org/10.1016/S1359-6454(98)00059-7.

[10] S.J. Andersen, Quantification of the Mj2Si/3" and/3' phases by transmission electron microscopy, Metall. Mater. Trans. 26 (1995) 1931–1937.

[11] J. Buha, R.N. Lumley, A.G. Crosky, K. Hono, Secondary precipitation in an Al-Mg-Si-Cu alloy, Acta Mater. 55 (2007) 3015–3024, https://doi.org/10.1016/j.actamat.2007.01.006.

[12] M.A. van Huis, J.H. Chen, H.W. Zandbergen, M.H.F. Sluiter, Phase stability and structural relations of nanometer-sized, matrix-embedded precipitate phases in Al-Mg-Si alloys in the late stages of evolution, Acta Mater. 54 (2006) 2945–2955, https://doi.org/10.1016/j.actamat.2006.02.034.

[13] V. Massardier, T. Epicier, Study of influence of low copper addition and of an excess of silicon on the precipitation kinetics and on the precipitation sequence of Al-Mg2Si alloys, Mater. Sci. Forum (2002) 396–402, https://doi.org/10.1007/978-1-4614-7990-1, 851–856.

[14] C. Cayron, P.A. Buffat, Transmission electron microscopy study of the β′ phase (Al-Mg-Si alloys) and QC phase (Al-Cu-Mg-Si alloys): ordering mechanism and crystallographic structure, Acta Mater. 48 (2000) 2639–2653, https://doi.org/10.1016/S1359-6454(00)00057-4.

[15] V. Garric, K. Colas, P. Donnadieu, G. Renou, S. Urvoy, B. Kapusta, Correlation between quenching rate, mechanical properties and microstructure in thick sections of Al–Mg–Si(–Cu) alloys, Mater. Sci. Eng. 753 (2019) 253–261, https://doi.org/10.1016/j.msea.2019.03.045.

[16] M. Jelani, Z. Li, Z. Shen, M. Sardar, Thermomechanical response of aluminum alloys under the combined action of tensile loading and laser irradiations, Chin. Phys. B 27 (2018), https://doi.org/10.1088/1674-1056/27/3/037901.

[17] C.Y. Cui, T.Y. Wan, Y.X. Shu, S. Meng, X.G. Cui, J.Z. Lu, Y.F. Lu, Microstructure evolution and mechanical properties of aging 6061 Al alloy via laser shock processing, J. Alloys Compd. 803 (2019) 1112–1118, https://doi.org/10.1016/j.jallcom.2019.06.347.

[18] Y. Wang, Y. Zhao, X. Xu, D. Pan, W. Jiang, X. Chong, Simultaneously enhanced strength and ductility of Al-Mg-Si alloys during aging process induced by electro-pulsing treatment, Materials 12 (2019), https://doi.org/10.3390/ma12091383.

[19] K. El-Menshawy, A.W.A. El-Sayed, M.E. El-Bedawy, H.A. Ahmed, S.M. El-Raghy, Effect of aging time at low aging temperatures on the corrosion of aluminum alloy 6061, Corros. Sci. 54 (2012) 167–173, https://doi.org/10.1016/j.corsci.2011.09.011.

[20] F. Eckermann, T. Suter, P.J. Uggowitzer, A. Afseth, P. Schmutz, The influence of MgSi particle reactivity and dissolution processes on corrosion in Al-Mg-Si alloys, Electrochim. Acta 54 (2008) 844–855, https://doi.org/10.1016/j.electacta.2008.05.078.

[21] N. Birbilis, R.G. Buchheit, Electrochemical characteristics of intermetallic phases in aluminum alloys, J. Electrochem. Soc. 152 (2005) B140, https://doi.org/10.1149/1.1869984.

[22] C. Blanc, G. Mankowski, Susceptibility to pitting corrosion of 6056 aluminium alloy, Corros. Sci. 39 (1997) 949–959, https://doi.org/10.1016/S0010-938X(97)81160-2.

[23] V. Guillaumin, G. Mankowski, Localized corrosion of 6056 T6 aluminium alloy in chloride media, Corros. Sci. 42 (2000) 105–125, https://doi.org/10.1016/S0010-938X(98)00116-4.

[24] J.M.C. Mol, J. Van De Langkruis, J.H.W. De Wit, S. Van Der Zwaag, An integrated study on the effect of pre- and post-extrusion heat treatments and surface treatment on the filiform corrosion properties of an aluminium extrusion alloy, Corros. Sci. 47 (2005) 2711–2730, https://doi.org/10.1016/j.corsci.2004.11.003.

[25] Y. Ma, X. Zhou, W. Huang, G.E. Thompson, X. Zhang, C. Luo, Z. Sun, Localized corrosion in AA2099-T83 aluminum-lithium alloy: the role of intermetallic particles, Mater. Chem. Phys. 161 (2015) 201–210, https://doi.org/10.1016/j.matchemphys.2015.05.037.

[26] E. Linardi, J. Collet-Lacoste, L. Lanzani, Characterization of AA6061 alloy oxides obtained in high Purity water and in diluted NaCl solution, Procedia Mater. Sci. 8 (2015) 56–64, https://doi.org/10.1016/j.mspro.2015.04.048.

[27] J. Huang, D. Lister, S. Uchida, L. Liu, The corrosion of aluminium alloy and release of intermetallic particles in nuclear reactor emergency core coolant: implications for clogging of sump strainers, Nucl. Eng. Technol. 51 (2019) 1345–1354, https://doi.org/10.1016/j.net.2019.02.012.

[28] E. Linardi, R. Haddad, L. Lanzani, Stability analysis of the Mg2Si phase in AA 6061 aluminum alloy, Procedia Mater. Sci. 1 (2012) 550–557, https://doi.org/10.1016/j.mspro.2012.06.074.

[29] M. Takeda, F. Ohkubo, T. Shirai, K. Fukui, Stability of metastable phases and microstructures in the ageing process of Al-Mg-Si ternary alloys, J. Mater. Sci. 33 (1998) 2385–2390, https://doi.org/10.1023/A:1004355824857.

[30] C. Badini, F. Marino, DSC study of ageing sequence in 6061aluminum alloy-SiC whiskers composite, Mater. Chem. Phys. 25 (1990) 57–70.

[31] C.D. Marioara, S.J. Andersen, H.W. Zandbergen, R. Holmestad, The influence of alloy composition on precipitates of the Al-Mg-Si system, Metall. Mater. Trans. A Phys. Metall. Mater. Sci. 36 (2005) 691–702, https://doi.org/10.1007/s11661-005-1001-7.

[32] I. Dutta, S.M. Allen, A calorimetric study of precipitation in commercial aluminium alloy 6061, J. Mater. Sci. Lett. 10 (1991) 323–326, https://doi.org/10.1007/BF02670289.

[33] S. Zajac, B. Bengtsson, C. Jönsson, Influence of cooling after homogenisation and reheating to extrusion on extrudability and final properties of AA 6063 and AA6082 alloys, Mater. Sci. Forum (2002) 396–402. https://doi.org/10.4028/www.scientific.net/msf.396-402.399, 399–404.

[34] L. Sagalowicz, G. Lapasset, G. Hug, Transmission electron microscopy study of a precipitate which forms in the Al-Mg-Si system, Phil. Mag. Lett. 74 (1996) 57–66, https://doi.org/10.1080/095008396180407.

[35] M.H. Jacobs, The structure of the metastable precipitates formed during ageing of an Al-Mg-Si alloy, Philos. Mag. 26 (1972) 1–13, https://doi.org/10.1080/14786437208221015.

[36] J.A. Vargas, J.E. Torres, J.A. Pacheco, R.J. Hernandez, Analysis of heat input effect on the mechanical properties of Al-6061-T6 alloy weld joints, Mater. Des. 52 (2013) 556–564, https://doi.org/10.1016/j.matdes.2013.05.081.

[37] I. Dutta, S.M. Allen, J.L. Hafley, Effect of reinforcement on the aging response of cast 6061 Al-Al2O3 particulate composites, Metall. Trans. A, Phys. Metall. Mater. Sci. 22A (1991) 2553–2563, https://doi.org/10.1007/BF02851349.

[38] R. Braun, Investigations on the long-term stability of 6013-T6 sheet, Mater. Char. 56 (2006) 85–95, https://doi.org/10.1016/j.matchar.2005.03.006.

[39] H.Q. Wang, W.L. Sun, Y.Q. Xing, Microstructure analysis on 6061 aluminum alloy after casting and diffuses annealing process, Phys. Procedia. 50 (2013) 68–75, https://doi.org/10.1016/j.phpro.2013.11.013.

[40] B. Milkereit, N. Wanderka, C. Schick, O. Kessler, Continuous cooling precipitation diagrams of Al-Mg-Si alloys, Mater. Sci. Eng. 550 (2012) 87–96, https://doi.org/10.1016/j.msea.2012.04.033.

[41] W.S. Ebhota, T.-C. Jen, Intermetallics formation and their effect on mechanical properties of Al-Si-X alloys, Intermet. Compd. - Form. Appl. (2018), https://doi.org/10.5772/intechopen.73188.

[42] C. Badini, F. Marino, A. Tomasi, Natural aging characteristics of aluminium alloy 6061 reinforced with SiC whiskers and particles, Mater. Sci. Eng. 136 (1991) 99–107, https://doi.org/10.1016/0921-5093(91)90445-S.

[43] J. Wloka, S. Virtanen, Microstructural effects on the corrosion behavior of high-strength Al-Zn-Mg-Cu alloys in an overaged condition, J. Electrochem. Soc. 154 (2007) 411–423, https://doi.org/10.1149/1.2742792.

[44] Z. Szklarska-Smialowska, Insight into the pitting corrosion behavior of aluminum alloys, Coi'rosion Sci. 33 (1992) 1193–1202. http://ac.els-cdn.com.manchester.idm.oclc.org/0010938X9290130U/1-s2.0-0010938X9290130U-main.pdf?_tid=e81aefc2-657e-11e7-841b-00000aacb35f&acdnat=1499698319_4df8eb9d0f9d8d25160620a859ff6b10.

[45] G.S. Chen, M. Gao, R.P. Wei, Microconstituent-Induced pitting corrosion in aluminum alloy 2024-T3, Corrosion 52 (1996) 8–15, https://doi.org/10.5006/1.3292099.

[46] A. Davoodi, J. Pan, C. Leygraf, S. Norgren, Probing of local dissolution of Al-alloys in chloride solutions by AFM and SECM, Appl. Surf. Sci. 252 (2006) 5499–5503, https://doi.org/10.1016/j.apsusc.2005.12.023.

[47] T.T.M. Tran, B. Tribollet, E.M.M. Sutter, New insights into the cathodic dissolution of aluminium using electrochemical methods, Electrochim. Acta (2016), https://doi.org/10.1016/j.electacta.2016.09.011.

[48] W. Zhang, S. Ruan, D.A. Wolfe, G.S. Frankel, Statistical model for intergranular corrosion growth kinetics, Corros. Sci. 45 (2003) 353–370, https://doi.org/10.1016/S0010-938X(02)00090-2.

[49] G. Svenningsen, M.H. Larsen, J.H. Nordlien, K. Nisancioglu, Effect of high temperature heat treatment on intergranular corrosion of AlMgSi(Cu) model alloy, Corros. Sci. 48 (2006) 258–272, https://doi.org/10.1016/j.corsci.2004.12.003.

[50] P. Schumacher, S. Pogatscher, M.J. Starink, C. Schick, V. Mohles, B. Milkereit, Quench-induced precipitates in Al-Si alloys: calorimetric determination of solute content and characterisation of microstructure, Thermochim. Acta 602 (2015) 63–73, https://doi.org/10.1016/j.tca.2014.12.023.

[51] T. Hagyard, W.B. Earl, Potential of aluminum in Aqueous chloride solutions, J. Electrochem. Soc. 114 (1967) 694, https://doi.org/10.1149/1.2426708.

[52] T. Hagyard, W.B. Earl, K.J. Kirkpatrick, I.G. Watson, The electrode potential of evaporated aluminum films in chloride solution, J. Electrochem. Soc. 113 (1966) 962, https://doi.org/10.1149/1.2424170.

[53] H.S. Isaacs, C. Scheffey, R. Huang, The location of events producing potential transients during pitting of freely corroding Al and its alloys, ECS Trans 11 (2008) 1–12, https://doi.org/10.1149/1.2925257.

[54] R. Ly, A.I. Karayan, K.T. Hartwig, H. Castaneda, Insights into the electrochemical response of a partially recrystallized Al-Mg-Si alloy and its relationship to corrosion events, Electrochim. Acta 308 (2019) 35–44, https://doi.org/10.1016/j.electacta.2019.03.220.

[55] R.G. Kelly, J.R. Scully, D.W. Shoesmith, R.G. Buchheit, Electrochemical Techniques in Corrosion Science and Engineering, Marcel Dekker, New York, 2003, https://doi.org/10.1016/s0013-4686(02)00768-5.